


RESEARCH

Open Access



Grading assessment of steel bar corrosion in concrete structures based on naive Bayesian model and spontaneous magnetic flux leakage effect

Beian Li¹, Shidong Li¹, Guangzhao Zhang¹, Huajian Ying², Qianwen Xia² and Shangkai Liu^{2*} 

*Correspondence:
skliu@mails.cqjtu.edu.cn

¹ Guangxi Xinxiang Expressway Co., Ltd., Nanning 530000, China

² College of Civil Engineering, Chongqing Jiaotong University, Chongqing 400074, China

Abstract

In order to explore an accurate method to evaluate the corrosion of reinforced concrete structures, the spontaneous magnetic flux leakage (SMFL) signal distribution on the surface of reinforced concrete specimens under different corrosion degrees was scanned based on SMFL technology. The influence of steel bar length, steel bar diameter, and other parameters on the distribution of SMFL signal was studied. The correlation between steel bar corrosion and the characteristic magnetic index of concrete structure was explored. Based on the naive Bayesian model, the classification evaluation of the steel bar corrosion degree of concrete structure was carried out. The results show that the variation of SMFL signal is affected by the corrosion degree α . When the lift-off height and the thickness of concrete protective layer remain unchanged, the slope between the peak and trough of B_z (magnetic induction intensity along z direction) curve increases with the increase of α , and the trough of B_x (magnetic induction intensity along x direction) curve decreases with the increase of the corrosion degree α . The peak and trough of magnetic signal curve can be used as the basis for determining the corrosion position. There is a strong correlation between the magnetic characteristic index β , γ , and the steel corrosion degree α obtained by SMFL. Through the characterization relationship between α , β , and γ , the corresponding models of single and comprehensive index β and γ were established. The results showed that the accuracy of β and γ integrated discriminant Naive Bayesian model-III reached 90.7%, which proved that the evaluation method has high reliability. This study explores the application of SMFL in corrosion detection of concrete structures.

Keywords: Spontaneous magnetic flux leakage effects, Concrete beam structures, Rust detection, Naive Bayesian model, Magnetic dipole model

Introduction

The safety and durability of bridges and their attached structures is a crucial field of bridge engineering research [1]. Due to the potential impact on the structure's bearing capacity, the corrosion of metal components has become a research hotspot [2].

Currently, the detection of steel corrosion in reinforced concrete is mainly based on electrochemical and physical methods.

As a non-destructive method, the electrochemical method has advantages such as high sensitivity, fast test speed, and local measurement, but its measurement has many influential factors, complicated analysis, and lack of quantification [3]. The physical method (mainly including the infrared thermal imaging detection technology, X-ray detection technology, etc. [4].) reflects the corrosion of reinforcing steel by measuring the change of physical properties caused by the corrosion of reinforcing steel. The infrared thermal imaging detection technology has high detection accuracy, fast detection speed, and wide detection range, but it is difficult to accurately quantify the depth of defects [5]. X-ray detection technology has high detection accuracy and it has high detection efficiency, but X-ray radiation has a great impact on the human body [6]. For applying non-destructive testing of steel corrosion in concrete structures, factors such as the testing theory's accuracy, the testing equipment's complexity, and the feasibility of long-term use need to be considered. Compared with other detection, SMFL detection technology can compensate for other detection methods' shortcomings.

The SMFL detection technology collects the magnetic leakage signals emitted by ferromagnetic materials at rust, damage, and microcracks according to the magnetic memory properties of metals. It can diagnose the presence of defects or stress concentrations in components by detecting and analyzing the surface leakage magnetic field strength of ferromagnetic components and its change characteristics and locates the location of the defects at the same time [7]. Compared with other nondestructive testing technologies, the SMFL testing technology can not only detect the macro defects of components but also detect the micro damage caused by internal stress concentration. It also has outstanding advantages such as high efficiency, simplicity, low cost, and strong applicability. It has extremely important research value and economic significance in the field of non-destructive testing of reinforcement corrosion in concrete structures [8].

For the magnetic inspection of reinforced concrete structures using leakage detection techniques, researchers have conducted in-depth studies in recent years. Orbe proposed a magnetic-based approach to evaluate the mechanical properties of steel fiber concrete [9]. H. Zhang et al. investigated the correlation between SMFL characteristic signals and structural corrosion of reinforced concrete [10]. J. Zhang et al. studied the qualitative and quantitative relationship between the corrosion rate of steel bars and magnetic induction strength [11]. Polydorides used tomography to analyze the magnetic induction intensity of the rusted reinforced concrete column itself [12]. Sun et al. used a concrete pile with a bored-in-place process and analyzed the magnetic anomalies of its internal reinforcement and summarized the relevant characteristics [13]. Szielasko et al. implemented the detection of reinforcement corrosion in reinforced concrete columns based on the MFL method [14]. Titus realized the corrosion detection of prestressed steel strands of prestressed concrete box girder bridges based on the MFL method [15]. Gaydecki et al. introduced the effective nondestructive magnetic imaging and condition assessment method of steel bars in detail [16]. Benitez et al. introduced in detail the effective non-destructive magnetic imaging and state assessment method of steel bars in prestressed concrete structures [17]. Zhang et al. and Liu et al. explored the assessment method for the degree of corrosion through

in-depth research on the SMFL signal characteristics of corroded reinforced concrete beams [18, 19]. Pang et al. proposed a method based on SMFL curve characteristics based on the previous research on the tensile test of outsourced concrete specimens to realize the calculation and correction of the stress in the reinforcement stage [20, 21]. Yang et al. based on SMFL completed the related research on the quantitative assessment of the corrosion degree of corroded steel bars [22]. Zhao explored the influence of steel bar diameter on the corrosion SMFL signal through in-depth research on the internal corrosion of corroded concrete specimens [23].

However, a unified standard for calculating the corrosion degree of reinforced concrete structures is yet to be determined by SMFL detection technology. The existing methods can only reflect the corrosion grade to a certain extent. Therefore, it is very important to explore a corrosion evaluation method that can be efficient, simple, nondestructive, and quantitative, and establish a quantitative evaluation system applicable to this method. In order to realize the evaluation of reinforcement corrosion in concrete structures, this paper takes the corroded reinforcement of concrete structures as the object of a series of test studies. Further, it explores the classification evaluation method of reinforcement corrosion of concrete structures.

Theoretical background

Three-dimensional magnetic dipole model

A three-dimensional magnetic dipole model is established to simulate the defect shape in the corroded area of the steel bar. The three-dimensional magnetic dipole corroded fault model of the trapezoidal groove is shown in Fig. 1. For the convenience of calculation, the circular cross-section with diameter d is transformed into a rectangular section with side length d , and the steel length is $2l$. The notch is placed in the center of the rebar as a trapezoidal notch. The bottom and top of the notch are $2c$ in the x direction, and the bottom is $2a$ in the y direction. The top of the notch is $2a+2b$ in the y direction, and the depth is h along the z direction.

Assume that the x — y plane is on the upper surface of the steel bar, and the origin is located at the geometric center of the top surface of the notch. At the ends of both sides

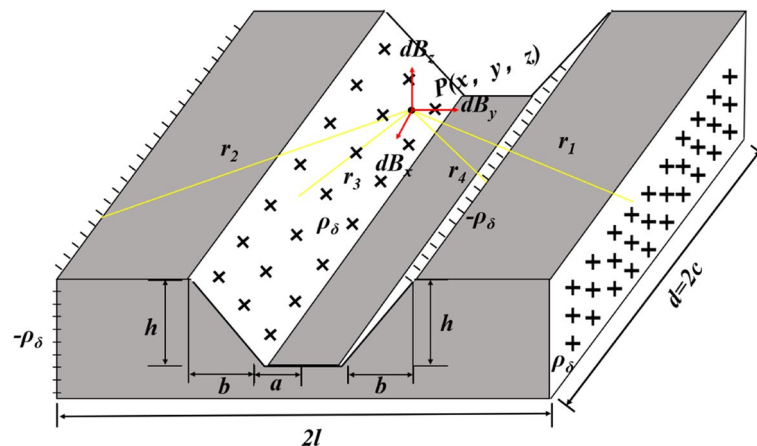


Fig. 1 Three-dimensional magnetic dipole corrosion fault model of trapezoidal groove part

of the steel bar, with the depth η along the x direction and the depth λ along the y direction as the center. There is a surface magnetic charge with a length along the x direction of $d\eta$, a height along the y -axis direction of $d\lambda$, and a magnetic charge density of ρ_{ms} . The magnetic field generated by the surface magnetic charge at any point $P(x,y,z)$ in space is shown in Eq. (1):

$$\begin{cases} \vec{dB}_1 = \begin{bmatrix} dB_{1x} \\ dB_{1y} \\ dB_{1z} \end{bmatrix} = \frac{-\rho_{ms}ds}{2\pi\mu_0r_1^3} \vec{r}_1 = \frac{-\rho_{ms}d\lambda d\eta}{2\pi\mu_0[(x-\eta)^3+(y-l)^3+(z+\lambda)^3]} \begin{pmatrix} |x-\eta| \\ y-l \\ z+\lambda \end{pmatrix} \\ \vec{dB}_2 = \begin{bmatrix} dB_{2x} \\ dB_{2y} \\ dB_{2z} \end{bmatrix} = \frac{\rho_{ms}ds}{2\pi\mu_0r_2^3} \vec{r}_2 = \frac{\rho_{ms}d\lambda d\eta}{2\pi\mu_0[(x-\eta)^3+(y+l)^3+(z+\lambda)^3]} \begin{pmatrix} |x-\eta| \\ y+l \\ z+\lambda \end{pmatrix} \end{cases} \quad (1)$$

The magnetization causes the two sidewalls of the trapezoidal slot to form two magnetic charge surfaces. On the charge surface, the charge is a surface of opposite polarity and equal charge density, assuming no charge distribution on the bottom surface of the trapezoid groove. Then, the left and right sides of the groove wall are centered on the depth η along the x direction and the depth δ along the z direction, the length along the x direction is $d\eta$, the height along the z axis direction is $d\delta$, and the width along the side wall direction is $(b^2+h^2)^{-1/2}hd\delta$. It is assumed that the internal magnetization of the steel bar is uniform, the surface magnetic charge is ρ_{ms} , and the vacuum permeability is $\mu_0=4\pi\times 10^{-7}H/m$. From these two surface magnetic charges at any point in space $P(x,y,z)$ generated by the magnetic field strength, as shown in Eq. (2):

$$\begin{cases} \vec{dB}_3 = \begin{bmatrix} dB_{3x} \\ dB_{3y} \\ dB_{3z} \end{bmatrix} = \frac{\rho_{ms}ds}{2\pi\mu_0r_3^3} \vec{r}_3 = \frac{\rho_{ms}\sqrt{1+b^2/h^2}d\delta d\eta}{2\pi\mu_0[(x-\eta)^3+(y+a+b-\delta b/h)^3+(z+\delta)^3]} \begin{pmatrix} |x-\eta| \\ y+a+b-\delta b/h \\ z+\delta \end{pmatrix} \\ \vec{dB}_4 = \begin{bmatrix} dB_{4x} \\ dB_{4y} \\ dB_{4z} \end{bmatrix} = -\frac{\rho_{ms}ds}{2\pi\mu_0r_4^3} \vec{r}_4 = -\frac{\rho_{ms}\sqrt{1+b^2/h^2}d\delta d\eta}{2\pi\mu_0[(x-\eta)^3+(y-a-b+\delta b/h)^3+(z+\delta)^3]} \begin{pmatrix} |x-\eta| \\ y-a-b+\delta b/h \\ z+\delta \end{pmatrix} \end{cases} \quad (2)$$

The SMFL signal intensity components B_x , B_y , B_z can be obtained by integrating along the x , y , and z directions respectively, as shown in Eq. (3):

$$\begin{cases} B_x = \int_{-c}^c d\eta \int_{-d}^0 dB_{1x} + \int_{-c}^c d\eta \int_{-d}^0 dB_{2x} + \int_{-c}^c d\eta \int_{-h}^0 dB_{3x} + \int_{-c}^c d\eta \int_{-h}^0 dB_{4x} \\ B_y = \int_{-c}^c d\eta \int_{-d}^0 dB_{1y} + \int_{-c}^c d\eta \int_{-d}^0 dB_{2y} + \int_{-c}^c d\eta \int_{-h}^0 dB_{3y} + \int_{-c}^c d\eta \int_{-h}^0 dB_{4y} \\ B_z = \int_{-c}^c d\eta \int_{-d}^0 dB_{1z} + \int_{-c}^c d\eta \int_{-d}^0 dB_{2z} + \int_{-c}^c d\eta \int_{-h}^0 dB_{3z} + \int_{-c}^c d\eta \int_{-h}^0 dB_{4z} \end{cases} \quad (3)$$

Naive Bayesian model

Naive Bayesian (NBC) models use relevant probability theory and statistics to classify a sample dataset. The model does not consider the relationship between the features of the test samples, does not require a large number of test samples, and has high classification efficiency. Objectively, it avoids subjective bias caused by using only previous samples and also avoids overfitting caused by using only sample information [24].

The naive Bayesian model is based on Bayes' theorem, assuming that the terms of the features are independent of each other and learning the standard input probability distribution in the output through a training group. After learning based on the model, input X for searching and output Y with the maximum posterior probability. There is a

sample data set $D = \{d_1, d_2, \dots, d_n\}$, the characteristic attribute set of the corresponding sample data is $X = \{x_1, x_2, \dots, x_d\}$, and the class variable is $Y = \{y_1, y_2, \dots, y_m\}$, that is, D can be divided into y_m categories. Where x_1, x_2, \dots, x_d are independent and random, the prior probability of Y is $P_{\text{prior}} = P(Y)$, and the posterior probability of Y is $P_{\text{post}} = P(Y|X)$, which can be obtained by the naive Bayesian algorithm. The posterior probability can be calculated from the prior probability $P_{\text{prior}} = P(Y)$, the evidence $P(X)$, and the class conditional probability $P(Y|X)$ [25].

The class conditional probability $P(Y|X)$ is given in Eq. (4).

$$P(Y|X) = \frac{P(Y)P(X|Y)}{P(X)} \quad (4)$$

Since the naive Bayesian model has the property that the eigenquants are independent of each other. Given the category of y , Eq. (5) can be further obtained from Eq. (4).

$$P(X|Y = y) = \prod_{i=1}^d P(x_i|Y = y) \quad (5)$$

From the above two equations, the posterior probability can be calculated to obtain the calculation Eq. (6).

$$P_{\text{post}} = P(Y|X) = \frac{P(Y) \prod_{i=1}^d P(x_i|Y)}{P(X)} \quad (6)$$

Since the magnitude of $P(X)$ is fixed, it is sufficient to compare only the numerator part of the above equation when comparing the posterior probabilities. Thus, a naive Bayesian calculation of the sample data belonging to category y_i can be obtained, and the equation is given in (7).

$$P(y_i|x_1, x_2, \dots, x_d) = \frac{P(y_i) \prod_{j=1}^d P(x_j|y_i)}{\prod_{j=1}^d P(x_j)} \quad (7)$$

Methods

Experimental design

Preparation of test specimens

In this experiment, reinforced concrete specimens of different sizes are designed, and the structural form is single-reinforced concrete. The type of steel bar is HRB400 threaded steel bar, both ends are exposed, and the middle is wrapped with C30 concrete, with a range of 80cm. The diameter R of the steel bar is 12mm, 16mm, and 20mm. The length L is 100cm, 150cm, and 200cm, and the thickness C of the outer concrete protective layer is 3cm, 4cm, and 5cm. The width W of the design corrosion area along the reinforcement direction is 10cm and 15cm, respectively. The structure of the specimen is shown in Fig. 2.

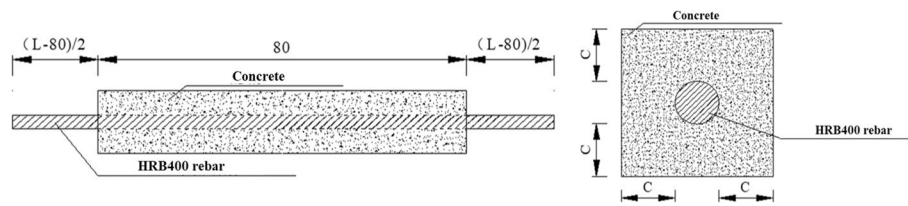


Fig. 2 Schematic diagram of the dimensions of the reinforced concrete structure specimen

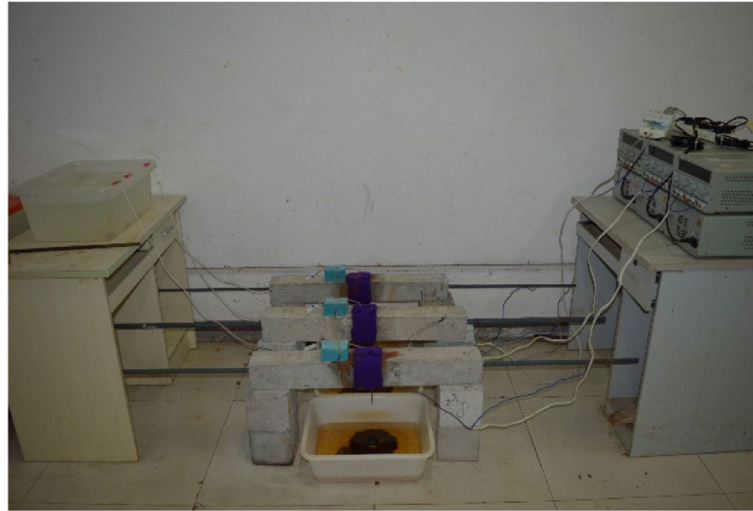


Fig. 3 Corrosion process diagram of reinforced concrete structure specimen

The specimen was corrupted by the electrochemical corrosion method. The reinforced concrete specimen was wrapped with an absorbent towel in the middle of the specimen and was always in a wet state so water could penetrate the concrete. The ATS3005S-3D dual DC power supply of ATTEN (Nanjing, China) was used to accelerate the corrosion of reinforced concrete specimens. Set the current constant to 1A. The positive electrode of the power supply connects the steel bar to oxidize it, and the negative electrode of the power supply connects the carbon rod to place the carbon rod in the towel. A 5% NaCl solution was prepared in the container as the electrolyte, and a siphon formed a closed current loop. The corrosion process of reinforced concrete structure specimens is shown in Fig. 3.

Reinforced concrete specimens of different sizes are named and distinguished by “L-C-R-W.” For example, “100-3-12-10” means the member is 100cm long, the outer concrete protective layer is 3cm thick, the steel bar diameter is 12mm, and the towel along the length of the steel bar covering the concrete corrosion width is 10cm. Each reinforced concrete specimen is corroded to different degrees. According to the preliminary pre-rust experiment, the shape of the rust zone obtained by this method is an approximately trapezoidal groove, similar to the three-dimensional magnetic dipole corrosion fault model with the trapezoidal groove in 2.1. In this test, the steel bars were corroded to different degrees by controlling the corrosion time (t/h). The specific working conditions are shown in Table 1.

Table 1 Rust condition

| Specimen model | Sample | Time t/h | Specimen model | Sample | Time t/h | Specimen model | Sample | Time t/h |
|----------------|--------|-------------|----------------|--------|-------------|----------------|--------|-------------|
| 100-3-12-10 | 1# | 12 | 150-3-12-10 | 19# | 48 | 200-3-12-10 | 37# | 84 |
| 100-3-12-15 | 2# | 12 | 150-3-12-15 | 20# | 48 | 200-3-12-15 | 38# | 84 |
| 100-3-16-10 | 3# | 12 | 150-3-16-10 | 21# | 48 | 200-3-16-10 | 39# | 84 |
| 100-3-16-15 | 4# | 12 | 150-3-16-15 | 22# | 48 | 200-3-16-15 | 40# | 84 |
| 100-3-20-10 | 5# | 12 | 150-3-20-10 | 23# | 48 | 200-3-20-10 | 41# | 84 |
| 100-3-20-15 | 6# | 12 | 150-3-20-15 | 24# | 48 | 200-3-20-15 | 42# | 84 |
| 100-4-12-10 | 7# | 24 | 150-4-12-10 | 25# | 60 | 200-4-12-10 | 43# | 96 |
| 100-4-12-15 | 8# | 24 | 150-4-12-15 | 26# | 60 | 200-4-12-15 | 44# | 96 |
| 100-4-16-10 | 9# | 24 | 150-4-16-10 | 27# | 60 | 200-4-16-10 | 45# | 96 |
| 100-4-16-15 | 10# | 24 | 150-4-16-15 | 28# | 60 | 200-4-16-15 | 46# | 96 |
| 100-4-20-10 | 11# | 24 | 150-4-20-10 | 29# | 60 | 200-4-20-10 | 47# | 96 |
| 100-4-20-15 | 12# | 24 | 150-4-20-15 | 30# | 60 | 200-4-20-15 | 48# | 96 |
| 100-5-12-10 | 13# | 36 | 150-5-12-10 | 31# | 72 | 200-5-12-10 | 49# | 108 |
| 100-5-12-15 | 14# | 36 | 150-5-12-15 | 32# | 72 | 200-5-12-15 | 50# | 108 |
| 100-5-16-10 | 15# | 36 | 150-5-16-10 | 33# | 72 | 200-5-16-10 | 51# | 108 |
| 100-5-16-15 | 16# | 36 | 150-5-16-15 | 34# | 72 | 200-5-16-15 | 52# | 108 |
| 100-5-20-10 | 17# | 36 | 150-5-20-10 | 35# | 72 | 200-5-20-10 | 53# | 108 |
| 100-5-20-15 | 18# | 36 | 150-5-20-15 | 36# | 72 | 200-5-20-15 | 54# | 108 |

The test platform

The test SMFL signal scanning adopts a three-dimensional magnetic scanning device to collect the spatial magnetic signal of the test piece. The automatic three-dimensional magnetic scanning device is composed of a control computer with a SMFL scanning control system, a three-axis mechanical displacement system, and a control cabinet. The control cabinet contains the stepping motor and programmable logic controller (PLC) inside, and the external is connected to the control computer through the serial port server. PLC can control the scanning system's moving rate and rest time through the computer input instruction to realize the detection automation. The control computer sends the SMFL scan instructions to the PLC and HMR2300 sensor through the serial port server, and then, the PLC sends the control instructions to the stepper motor. A stepping motor drives the three-axis automatic displacement system, and the three motors control the movement of the scanning device in three directions, respectively. Then, the digital information, such as displacement and SMFL signal, is processed by the serial port server and fed back to the control computer. HMR2300 is a 3D intelligent digital magnetometer produced by Honeywell Corporation in the USA. Its detection accuracy is $6.9 \times 10^{-2} mG$, and the range is $\pm 2Gs$. It can realize the acquisition of 3D space magnetic signals with controllable speed and path. HMR2300 is equipped with three reluctance sensors distributed in the X , Y , and Z directions. It can simultaneously detect the magnetic induction intensity in three dimensions of space and input the results to the control computer. Finally, it outputs the spatial coordinates X , Y , and Z of the data acquisition point on the scanning path and the distribution of the magnetic induction components B_x , B_y , and B_z , as shown in Fig. 4.

The three-axis micro-magnetic scanning system is used to collect the initial SMFL signals of each group of reinforced concrete structural specimens. As shown in Fig. 5, in

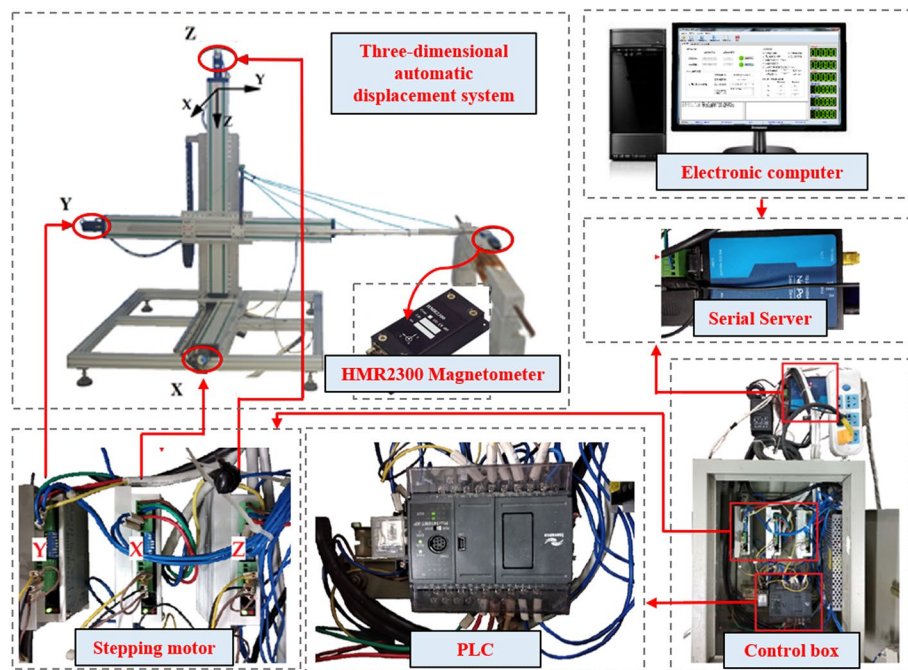


Fig. 4 Automated magnetic field scanning system

order to avoid the end effect of the steel bars, the start and stop positions of the Y direction scanning are set in the concrete-coated concrete 50mm outside the steel bar. The lift-off height of multiple magnetic signal probes is set to advance at a speed of 500mm per minute and continuously capture the magnetic flux. Scan the SMFL signal along the Z direction at the geometric center position of the specimen and at the positions of 100mm and 200mm apart on both sides, and rise from the center lifting height at a speed of 300mm per minute to a lift-off height of 705mm, both in 2s. One acquisition rate collects the SMFL signal above the specimen. Before the corrosion test, the scanning equipment performs the first magnetic signal acquisition to obtain the initial magnetic signal of the sample.

Results

Figure 6 shows the surface condition of each outsourced concrete reinforcement specimen after the test. After the corrosion is completed, the concrete on the surface of the reinforced concrete structure is chiseled with a tool hammer. Measuring the diameter of the uncorroded part and the minimum diameter of the corroded part of all the rebar with a vernier caliper, as shown in Fig. 7. After completion of corrosion according to the designed corrosion condition, the actual section corrosion degree “ α ” is calculated according to Formula (8), which is listed in Table 2.

$$\alpha = \frac{\Delta W}{W} = \frac{\pi l \rho \left\{ (R_o/2)^2 - \left[(R_o/2)^2 + (R_c/2)^2 + (R_o/2)(R_c/2) \right] / 3 \right\}}{\pi (R_o/2)^2 l \rho} = \left[2 - (R_c/R_o)^2 - (R_c/R_o) \right] / 3 \quad (8)$$

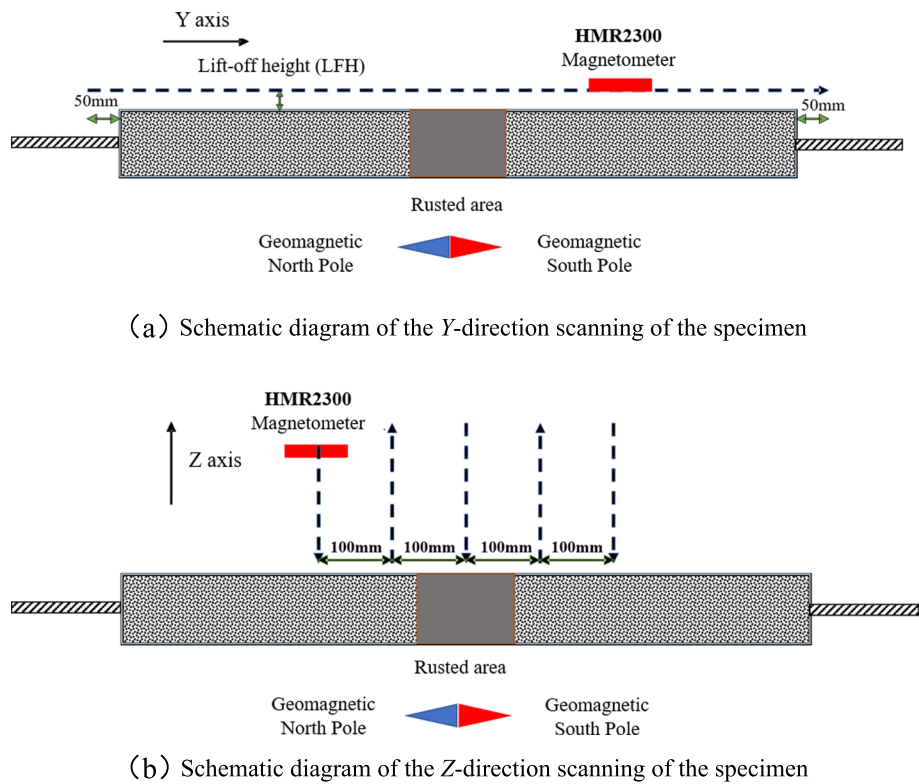


Fig. 5 Schematic diagram of magnetic flux leakage signal scanning of reinforced concrete structure specimen. **a** Schematic diagram of the Y-direction scanning of the specimen. **b** Schematic diagram of the Z-direction scanning of the specimen

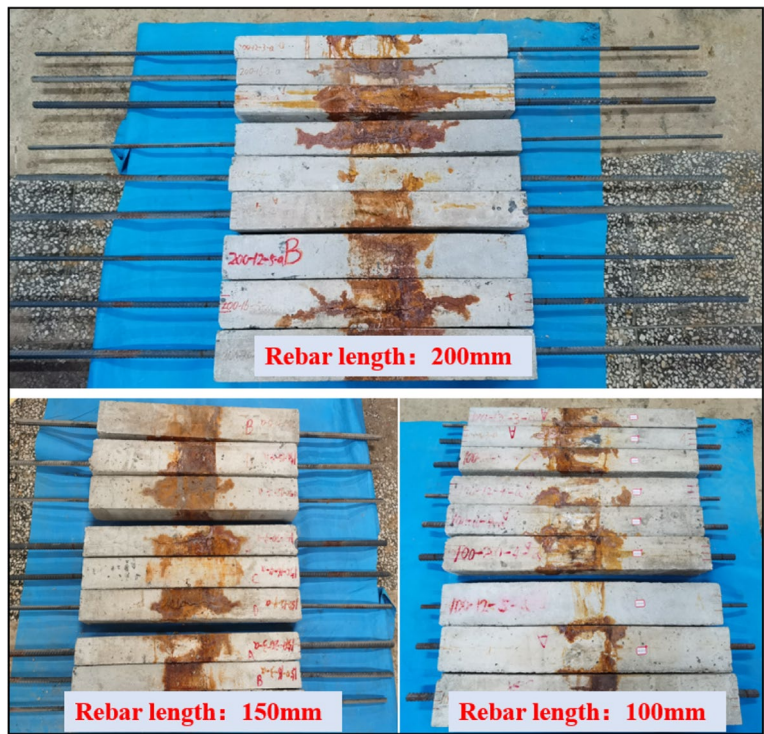


Fig. 6 Surface condition of corroded steel bar of concrete structure specimen

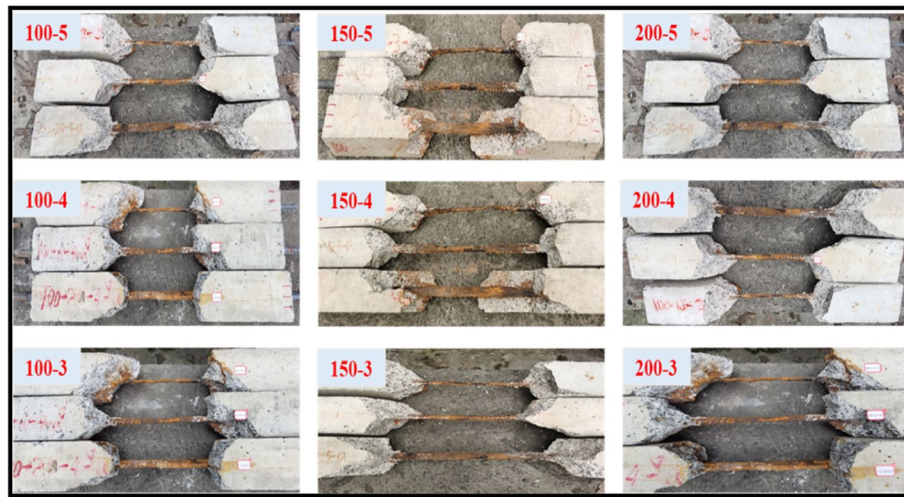


Fig. 7 Internal situation of steel bar corrosion of concrete structure specimen

Table 2 Corrosion degree of specimen

| Sample | α | Sample | α | Sample | α | Sample | α | Sample | α | Sample | α |
|--------|----------|--------|----------|--------|----------|--------|----------|--------|----------|--------|----------|
| 1# | 0.142 | 10# | 0.107 | 19# | 0.567 | 28# | 0.266 | 37# | 0.993 | 46# | 0.425 |
| 2# | 0.095 | 11# | 0.102 | 20# | 0.378 | 29# | 0.255 | 38# | 0.662 | 47# | 0.408 |
| 3# | 0.080 | 12# | 0.068 | 21# | 0.319 | 30# | 0.170 | 39# | 0.558 | 48# | 0.272 |
| 4# | 0.053 | 13# | 0.425 | 22# | 0.213 | 31# | 0.851 | 40# | 0.372 | 49# | 0.276 |
| 5# | 0.051 | 14# | 0.284 | 23# | 0.204 | 32# | 0.567 | 41# | 0.357 | 50# | 0.851 |
| 6# | 0.034 | 15# | 0.239 | 24# | 0.136 | 33# | 0.479 | 42# | 0.238 | 51# | 0.718 |
| 7# | 0.284 | 16# | 0.160 | 25# | 0.709 | 34# | 0.319 | 43# | 1.134 | 52# | 0.479 |
| 8# | 0.190 | 17# | 0.153 | 26# | 0.473 | 35# | 0.306 | 44# | 0.756 | 53# | 0.459 |
| 9# | 0.160 | 18# | 0.102 | 27# | 0.399 | 36# | 0.204 | 45# | 0.638 | 54# | 0.306 |

where ΔW represents the quality reduction of the steel bar after corrosion. W represents the quality of reinforcement before test. l represents the length of reinforcement corrosion interval. ρ represents the density of reinforcement. R_0 represents the measured diameter of the steel bar in the non-corroded area. R_c represents the minimum diameter of the corroded steel bar in the corroded area.

The magnetic signals before and after the corrosion of the specimen are analyzed. The results show that the magnetic induction intensity B_x in the X direction and B_z along the Z direction are more sensitive and regular to the corrosion of steel bars, so the distribution of the magnetic signals B_x and B_z is mainly analyzed.

Take 14# and 26# specimens as examples. As shown in Figs. 8 and 9, when the rust degree α is close to or equal to 0, the B_z curve of each lift-off height is monotonically decreasing and reaches the maximum value near both ends of the curve. The B_x curve of each lift-off height basically presents an envelope shape and the curves do not intersect with each other. The initial magnetic signal at the end of the specimen begins to change abruptly at the end, showing irregularity, which is mainly due to the partial damage and stress concentration of the specimen caused by the cutting of steel bars. When the rust degree α is larger than 0, the monotonicity of the B_z curve of each lift-off height changes

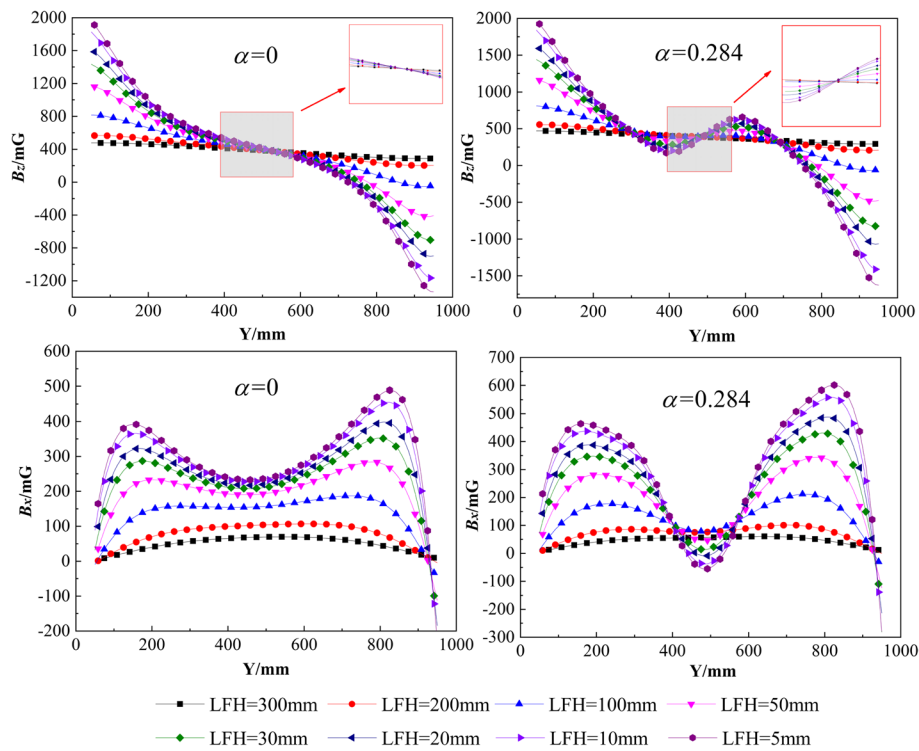


Fig. 8 B_z curve and B_x curve of specimen 14# before and after corrosion

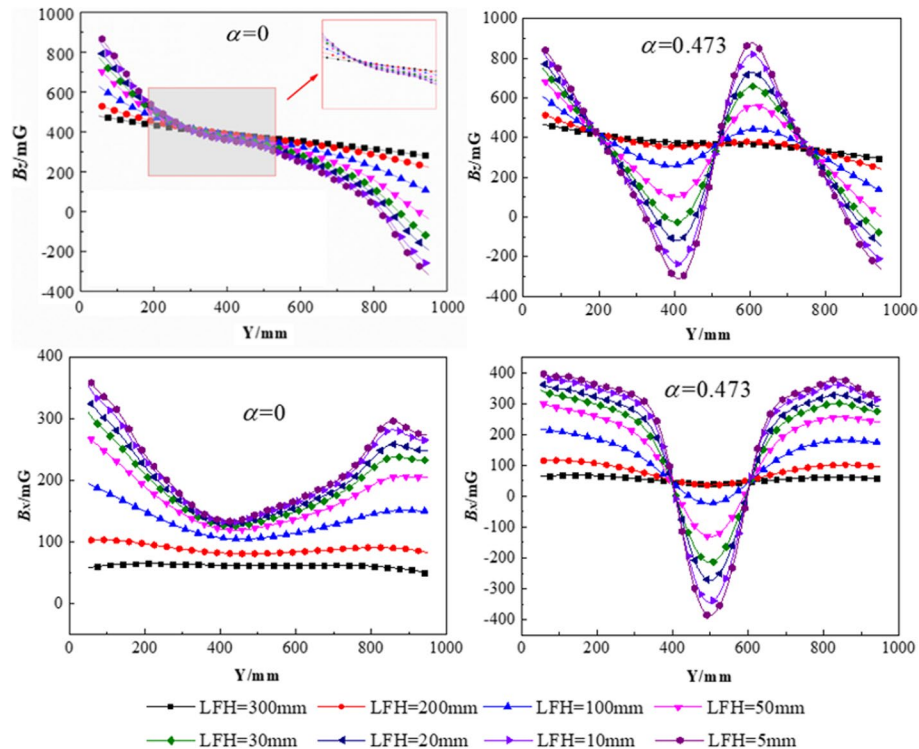


Fig. 9 B_z curve and B_x curve of specimen 26# before and after corrosion

in the rusted area. In the uncorroded area, it still decreases monotonically but increases monotonically at the rusted area. The slope of the curve increases with the lift-off height. The range between the new peaks and troughs can be used as the basis for judging the location of rust. The B_x curves of each lift-off height form a new trough in the rusted area, and also the range between the intersection points of each B_x curve can be used as the basis for determining the location of corrosion.

Under the premise of the same lift-off height, as the corrosion degree α increases, the B_z curve of the corroded area forms new peaks and troughs. The curve between the new crest and trough becomes more inclined with the increase of corrosion degree α . The higher the slope between the crest and trough, the higher the degree of corrosion, and the greater the change rate of the magnetic signal. As shown in Fig. 8 that the B_x curve of the rusted area forms a new wave trough, and the new wave trough decreases as the corrosion degree α increases. The uncorroded area basically maintains a similar trend, as shown in Figs. 8 and 9. With the increase of lift-off height, the change range of B_x and B_z curves gradually becomes gentle and gradually tends to a straight line. When the lift-off height of the acquisition device is 300mm, the influence of the corrosion degree of the specimen on the spontaneous flux leakage signal is small and can be approximately ignored. Although the initial magnetic field has been deducted, the magnetic signal of B_z is still close to 400mG due to the influence of the environmental magnetic field. In contrast, the magnetic signal of B_x is better, basically approaching 0mG.

Correlation analysis of corrosion and magnetic characteristic index

In order to realize the quantitative detection of reinforced concrete structures with different corrosion degrees, it is necessary to extract the characteristic magnetic index, which can reflect the corrosion degree α . Since the value of lift-off height (LFH) has a certain impact on the magnetic induction intensity B_x and B_z , therefore, when extracting the magnetic feature index, the LFH is uniformly taken as 5mm.

As shown in Fig. 10a, corrosion will change the gradient of the B_z curve from negative to positive. The slope β is defined to reflect the corrosion degree of the reinforced concrete structural specimen, and the slope β can be calculated from Eq. (9). As shown in Fig. 10b, the trough value $B_{x\max}$ can reflect the corrosion degree of the reinforced concrete structural specimen, but the reinforced concrete structural

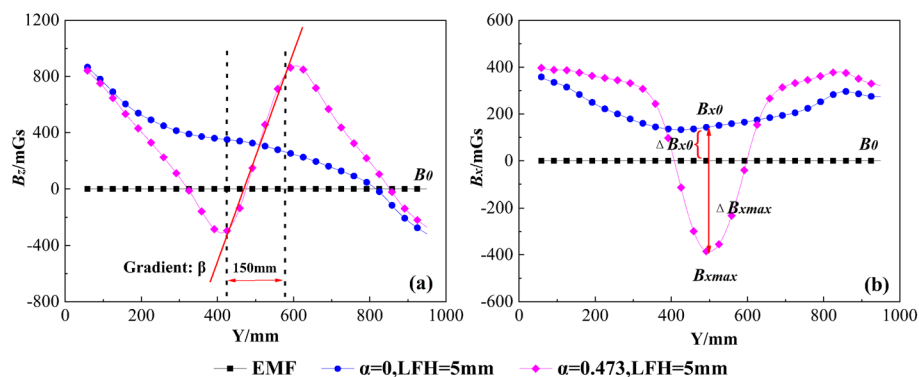


Fig. 10 Definition of magnetic characteristic index **a** β and **b** γ

specimens of different sizes have different initial magnetic fields. Therefore, the index γ is set and obtained by the definition of Eq. (10), where $\Delta B_{x\max}$ represents the magnetic field increment at the trough in the rusted area, $B_{x\max}$ is the magnetic induction intensity at the trough after rusting, B_{x0} is the magnetic induction intensity at this position before rusting, and B_0 is the magnetic induction intensity of the ambient magnetic field, which is usually a constant and is set to $0mG$.

Defining the magnetic characteristic metrics:

$$\beta = \max \{(B_{z1} - B_{z2}) / (Y_1 - Y_2)\} \quad (9)$$

$$\gamma = \frac{|\Delta \beta_{x\max}|}{|\Delta B_{x0}|} = \frac{|B_{x\max} - B_{x0}|}{|B_{x0} - B_0|} \quad (10)$$

Correlation analysis between rust degree α and magnetic characteristic index β

Taking reinforced concrete structure size “100-3-12-10” as an example, the magnetic characteristic index β at different lift-off heights is calculated, as shown in Fig. 11a. It can be seen from the figure that with the increase of lift-off height, the magnetic characteristic index β curve shows a decreasing trend, and the absolute value of the slope of the curve gradually decreases. When the lift-off height is small, the magnetic characteristic index β gradually increases with the increase of the rust degree. When the lift-off height reaches 300 mm, the magnetic characteristic index value β under each rust degree is close to a point. This is mainly because the influence of lift-off height on the magnetic characteristic index β is not considered.

Therefore, the index β of different lift-off heights is revised, as shown in Eqs. (11) and (12):

$$\lambda(z) = \frac{z + (r + c)}{z_0 + (r_0 + c_0)} \quad (11)$$

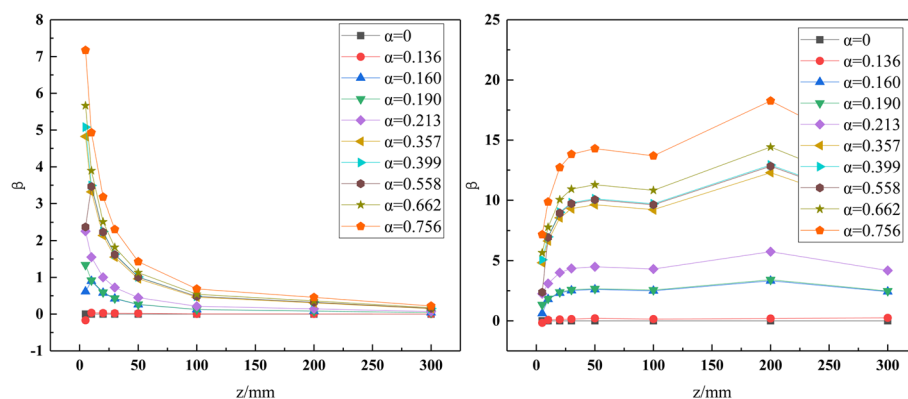


Fig. 11 The magnetic characteristic index β of the specimen under different lift-off heights. **a** β (not consider LFH). **b** β (consider LFH)

$$\beta = \beta|_{z=z_1} \bullet \lambda(z_1) \quad (12)$$

where $\beta|_{z=z_1}$ means that when the lift-off height is z_1 , the magnetic characteristic index value is obtained at this time, z_0 means the initial lift-off height, r means the radius of the steel bar, r_0 means the radius of the initial steel bar, c means the thickness of the protective layer of concrete, and c_0 represents the thickness of the initial concrete cover.

It can be seen from Fig. 11b that after considering the influence of lift-off height z and calculating the magnetic characteristic index β , the β curve changes. When the lifting height z is 0mm, the value of β after each corrosion degree correction is unchanged from before the correction in Fig. 11a. With the increase of lift-off height, the β curve of the steel bar with a low corrosion degree is basically horizontal, and the β curve of the steel bar with a high corrosion degree gradually increases first, and when the lift-off height z is higher than 200mm, the β curve gradually decreases. At the same lift-off height, the difference of rebar β with different corrosion degrees is almost proportional to the difference in corrosion degree α . It shows that the correction of magnetic characteristic index β is feasible and effective.

The corrosion degree α will be collected from the SMFL signal of a random number of reinforced concrete structural specimens at the lift-off height (LFH=5mm). The β value of the magnetic characteristic index is used to construct a magnetic characteristic matrix reflecting the corrosion degree α , and the α is characterized in two dimensions to improve the accuracy of quantitative identification. As shown in Fig. 12, with the increase of the corrosion degree α , the magnetic characteristic index β generally increases. However, it has some discreteness, but the discreteness is small, and the whole is relatively compact.

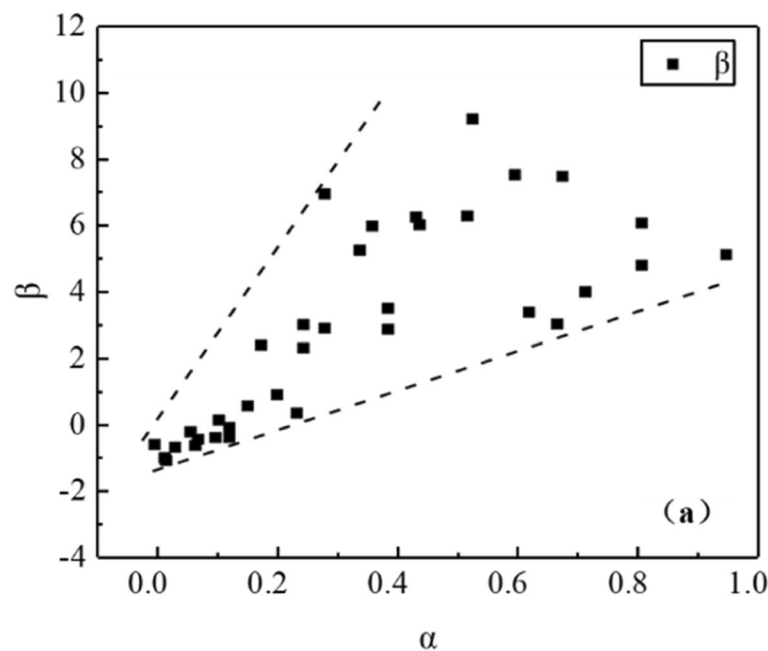


Fig. 12 Distribution of magnetic characteristic index value β

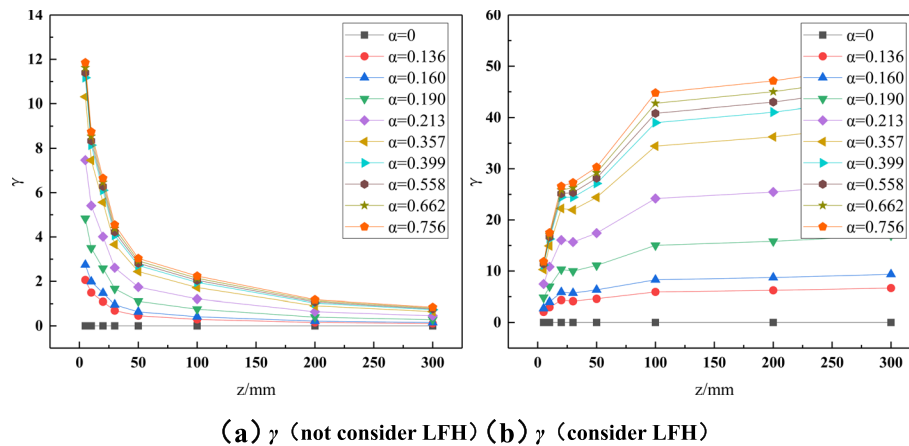


Fig. 13 The magnetic characteristic index γ of the specimen under different lift-off heights. **a** γ (not consider LFH). **b** γ (consider LFH)

Correlation analysis between rust degree α and magnetic characteristic index γ

The data of different lift-off heights of reinforced concrete structures are analyzed. The size of the reinforced concrete structure is also taken as an example of “100-3-12-10”. The magnetic characteristic index γ under different lift-off heights is calculated, and its variation law is analyzed, as shown in Fig. 13a. It can be seen from the figure that with the increase of lift-off height, the γ curve of the magnetic characteristic index is similar to the previous β curve and also shows a decreasing trend, and the absolute value of the slope of the curve gradually decreases. Under the condition of the same lift-off height, the larger the value of corrosion degree α , the larger the value of magnetic characteristic index γ . When the lift-off height z is larger, the value of the magnetic characteristic index γ tends to 0 under each rust degree. Therefore, it is necessary to modify the magnetic characteristic index considering the lift-off height z .

Modify the index γ of different lift-off heights, as shown in Formulas (11) and (13):

$$\gamma = \gamma|_{z=z_1} \bullet \lambda(z_1) \quad (13)$$

where $\gamma|_{z=z_1}$ means that when the lift-off height is z_1 , the magnetic characteristic index γ value is obtained at this time.

Considering the influence of the lift-off height z and calculating the magnetic characteristic index γ , Fig. 13b is obtained. From the figure, it can be obtained that when the lift-off height z is 0 mm, the specific value of γ under each rust degree is still the same as before. With the increase of the lift-off height, the γ curve of the less corroded steel bar is basically horizontal, while the β curve of the more corroded steel bar has a gradually increasing trend when the lift-off height z is 0–100 mm. It remains relatively flat in the 300-mm area. Under the same lift-off height z , the difference between steel bars β with different corrosion degrees is still proportional to the difference between the corrosion degrees α . The figure shows that the correction of the magnetic characteristic index γ is feasible.

Still control LFH=5mm, according to the method of obtaining β to extract, calculate and modify the magnetic signal to obtain the magnetic characteristic index γ value. The characteristic index γ value is used to construct a magnetic characteristic matrix reflecting the corrosion degree α , and the two-dimensional representation of α is carried out

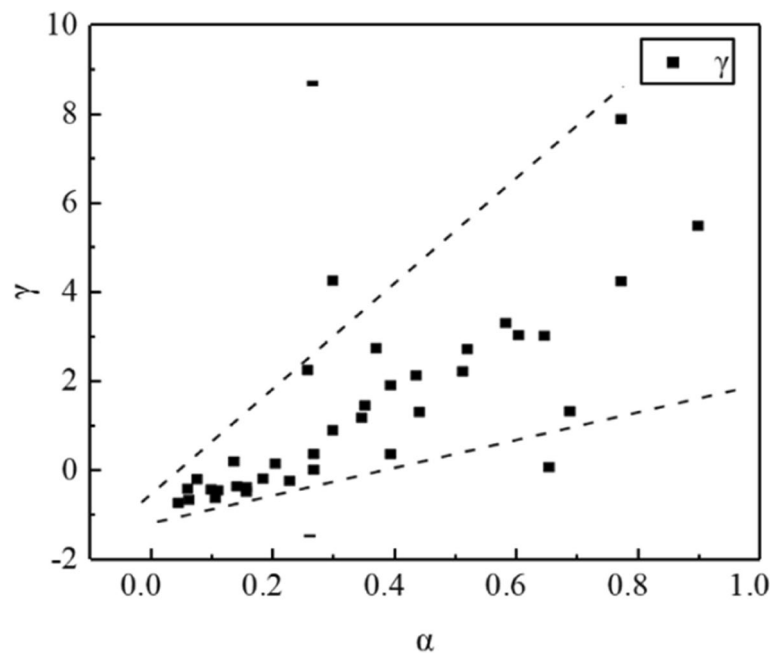


Fig. 14 Distribution of magnetic characteristic index value γ

to improve the accuracy of quantitative identification. As shown in Fig. 14, with the increase of the rust degree α , the magnetic characteristic index γ generally shows an upward trend, but there are different degrees of dispersion. Compared with the magnetic characteristic index β , the overall discrete type is larger.

Reliability of correlating the magnetic flux model with corrosion degree

Simulation analysis based on three-dimensional magnetic dipole model

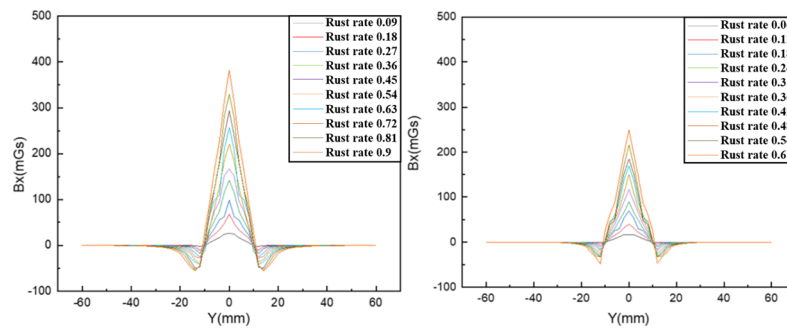
In order to analyze the influence of the magnetic dipole model in the corrosion assessment and detection, according to the Formula (14) of Faraday's first law of electrolysis, it can be obtained:

$$\Delta W = \frac{M}{nF} I \Delta t \quad (14)$$

$$W = \frac{\pi d^2 l \rho}{4} \quad (15)$$

$$\alpha = \frac{\Delta W}{W} \quad (16)$$

where ΔW represents the corrosion amount of the metal within Δt , Δt represents the corrosion time, M represents the molar mass of Fe, $M=56\text{g/mol}$, n represents the number of electrons lost by Fe during the oxidation process, where $n=2$, F represents the constant Faraday, $1F=96485\text{C}$, I represents the current flowing out of the anode, W represents the mass of the corroded area before corrosion, d represents the diameter of the



(a) 12mm diameter steel bar model calculation (b) 16mm diameter steel bar model calculation

Fig. 15 Simulation calculation of B_x component of flux leakage signal along Y -axis under different rust degrees. **a** 12-mm diameter steel bar model calculation. **b** 16-mm diameter steel bar model calculation

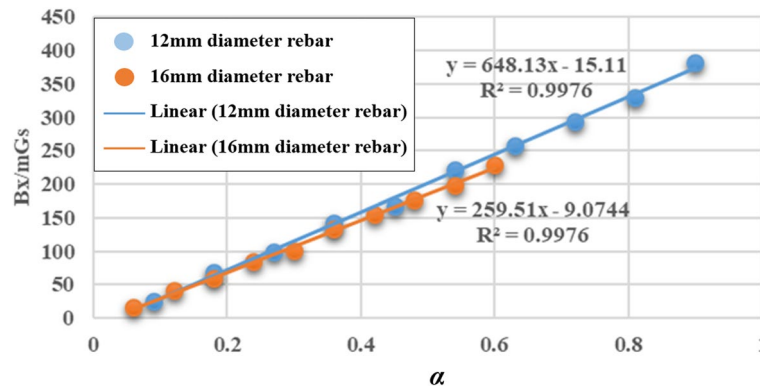


Fig. 16 Distribution of B_x extreme values of each model under different rust degrees

steel bar, l represents the width of the corroded area, $\rho=7800\text{g/mm}^3$. α represents the corrosion degree of steel bars, which is expressed by the loss rate of cross-sectional area.

According to Eqs. (14), (15), and (16), it can be known that the model stable current I is set to 1A, the time interval for each corrosion is 12h, and the diameter of the steel bar is divided into 12mm and 16mm. The area loss rate was used to obtain the corrosion degree of the steel bar. The finite element software MATLAB is used to simulate and calculate the changes of the tangential component B_x and the normal component B_z of the strength of the SMFL signal of the steel bar along the Y -axis direction under different corrosion degrees. The angle between the side surface and the bottom surface of the trapezoidal groove section is set to be 145° , and the parameter settings of the model are shown in Tables 5 and 6 in Appendix 1.

The tangential component of SMFL signal intensity was obtained by substituting the set experimental parameters into Eq. (3). Then, through MATLAB simulation calculation, the change of the tangential component of SMFL signal strength B_x along the Y -axis of the steel bar with two diameters under each degree of rust is drawn, as shown in Fig. 15a and b. It can be seen that the magnetic signal has a sudden change in the corrosion zone, and the magnetic signal's intensity increases with the corrosion degree increase. Besides, the tangential component B_x curve of the SMFL

Table 3 Classification of corrosion degree α of steel bars

| Rebar | No corrosion | Slight corrosion | Moderate corrosion | Severe corrosion |
|-------------------------|------------------------|--------------------------|-------------------------|--------------------------|
| Corrosion grade | 1 | 2 | 3 | 4 |
| Corrosion rate α | $0 \leq \alpha < 0.02$ | $0.02 \leq \alpha < 0.1$ | $0.1 \leq \alpha < 0.2$ | $0.2 \leq \alpha \leq 1$ |

Table 4 Model accuracy comparison

| Rebar condition | Corrosion grade | NBC-I | NBC-II | NBC-III |
|--------------------|-----------------|---------|---------|---------|
| No corrosion | 1 | 100.00% | 100.00% | 100.00% |
| Slight corrosion | 2 | 83.30% | 91.60% | 91.70% |
| Moderate corrosion | 3 | 77.80% | 56.60% | 83.30% |
| Severe corrosion | 4 | 83.30% | 91.70% | 95.60% |
| Overall accuracy | | 81.50% | 79.60% | 90.70% |

signal under different corrosion degrees intersects at the left and right two points, and the distance between the two intersection points is consistent with the set corrosion width. The results of the simulation analysis are in agreement with the test results obtained in the “Results” section. As shown in Fig. 16, under the two diameter models, the goodness of fit R^2 reaches 0.9976. The maximum value of tangential component B_x increases linearly with the increase of corrosion degree. It indicates that the three-dimensional magnetic dipole model can be used to detect and analyze the SMFL signal of reinforcement corrosion in concrete structures.

Rust grading evaluation based on naive Bayesian model

The current SMFL detection technology has no exact standard for the classification of the corrosion degree of steel bars. By drawing on the classification standard of the electrochemical method [26], and referring to the research results of previous researchers on the evaluation of the corrosion level of steel strands [27]. According to the corrosion degree α , the steel corrosion degree is classified into four grades, as shown in Table 3.

By analyzing and sorting out the relationship between the corrosion degree α and the magnetic characteristic indexes β and γ , the evaluation indexes describing the corrosion degree of the structure are summarized, and the steel corrosion evaluation system is put forward.

The Bayesian classification is used to achieve the classification of the corrosion degree of the bare bars. The magnetic characteristics β and γ are single indicators corresponding to the models NBC-I and NBC-II respectively, and the comprehensive indicators of the magnetic characteristics β and γ are corresponding to the model NBC-III. The accuracy of each model is shown in Tables 7, 8, and 9 in Appendix 2, and the comparison of the accuracy of the three models is shown in Table 4.

From Tables 7 and 8 in the Appendix 2, it can be seen that the accuracy of the magnetic characteristic index β and γ single index discrimination is close to 80%, and the overall evaluation system has a certain degree of reliability. But the single index has the lowest accuracy rate for judging the degree of moderate corrosion. Table 9 in Appendix 2 shows that the comprehensive discrimination accuracy rate of the magnetic characteristic

indicators β and γ exceeds 90%, which is 10% higher than that of a single indicator, especially the discrimination accuracy rate of moderate corrosion degree is increased by up to 50%. The evaluation system has high reliability.

Through the comparative analysis of the overall or individual accuracy, it is found that the three models can effectively evaluate the reinforcement without corrosion. The overall accuracy of model NBC-III is the highest, reaching 90.7%, which also verifies the reliability of grading evaluation of SMFL detection of reinforcement corrosion in concrete structures. Combining with Table 4, it can be seen that the model NBC-I has the highest accuracy rate in a single evaluation index, and the overall accuracy rate is higher than 80%. The model NBC-III has the highest accuracy rate among all models, and the overall accuracy rate exceeds 90%. The reliability of the model NBC-III is a graded assessment of the optimal model for the SMFL detection of steel bar corrosion in concrete structures.

Conclusions

Based on the SMFL detection technology and classification evaluation method, this paper carried out the SMFL detection test of steel bar corrosion in concrete structures. It also analyzed the variation law of the SMFL signal at the corrosion damage of the steel bar under different corrosion degrees α . Corrosion degree is related to the magnetic characteristic index, and a classification evaluation method of steel corrosion is proposed and its SMFL signal is analyzed. The naive Bayesian model is introduced to classify and evaluate the corrosion results of steel reinforcement in concrete structures, and the following conclusions are obtained:

- (1). After studying the law of the SMFL signal on the surface of the specimen after corrosion, it can be obtained that when the value of α is larger than 0, the monotonicity of the B_z curve of each lift-off height changes in the corrosion area. There will be a monotonically increasing phenomenon in the corrosion area, and new crests and troughs are formed near the corrosion area. The range between the new crests and troughs can be used as the basis for determining the location of corrosion. The B_x curves of each lift-off height form a new trough in the corrosion area, and the intersection of each curve. The range can be used as the basis for judging the location of corrosion.
- (2). Through the exploration of the magnetic induction intensity B_x and B_z before and after the corrosion of the component, the magnetic characteristic index values β and γ are defined. When the lift-off height is constant, β , γ , and the corrosion degree α of the steel bar have a strong correlation, as the two-dimensional magnetic eigenvalues that characterize α . With the increase of α , the magnetic eigenvalues β and γ show an overall increasing trend, but they also have a certain degree of discreteness.
- (3). A naive Bayesian model was used to establish an evaluation system between magnetic characteristic indexes β , γ , and steel corrosion grade. The accuracy of β and γ composite indexes to identify the corresponding model NBC-III was higher than that of β and γ single index to identify the corresponding model NBC-I and NBC-II, and the overall accuracy of model NBC-III was up to 90.7%.

Compared with NBC-I and NBC-II, the discriminant accuracy increased by 11.1%, and the discriminant accuracy of moderate rust degree increased by 50%. The evaluation system has high reliability.

To sum up, the conclusions of this paper confirm the reliability of the naive Bayesian model for the detection and evaluation of the corrosion degree of reinforced concrete. However, there are few influencing factors in the process of obtaining the above data, and the conclusions obtained will have many limitations when applied in practical engineering. More influencing factors need to be considered, such as temperature, humidity, bearing capacity, and other combined effects. Therefore, in order to truly apply the efficient and fast SMFL detection technology to practical engineering, it is necessary to consider as many influencing factors as possible from the perspective of experiments and improve the related mechanism and theoretical research.

Appendix 1

Tables 5 and 6.

Table 5 12-mm steel bar diameter model parameter settings (mm)

| Rust length l/mm | Concrete cover Thickness (mm) | Rust time T/h | Rust rate α | Rust depth h/mm | Rust width 2a+2b/mm |
|---------------------|-------------------------------------|---------------|--------------------|--------------------|------------------------|
| 100 | 6 | 12 | 0.09 | 1.70 | 13.40 |
| 100 | 6 | 24 | 0.18 | 3.40 | 16.80 |
| 100 | 6 | 36 | 0.27 | 5.10 | 20.21 |
| 100 | 6 | 48 | 0.36 | 6.81 | 23.61 |
| 100 | 6 | 60 | 0.45 | 8.51 | 27.01 |
| 100 | 6 | 72 | 0.54 | 10.21 | 30.42 |
| 100 | 6 | 84 | 0.63 | 11.91 | 33.82 |
| 100 | 6 | 96 | 0.72 | 13.61 | 37.22 |
| 100 | 6 | 108 | 0.81 | 15.31 | 40.63 |
| 100 | 6 | 120 | 0.90 | 17.01 | 44.03 |

Table 6 16-mm steel bar diameter model parameter settings (mm)

| Rust length l/mm | Concrete cover Thickness (mm) | Rust time T/h | Rust rate α | Rust depth h/mm | Rust width 2a+2b/mm |
|---------------------|-------------------------------------|---------------|--------------------|--------------------|------------------------|
| 100 | 8 | 12 | 0.06 | 1.70 | 13.40 |
| 100 | 8 | 24 | 0.12 | 3.40 | 16.80 |
| 100 | 8 | 36 | 0.18 | 5.10 | 20.21 |
| 100 | 8 | 48 | 0.24 | 6.81 | 23.61 |
| 100 | 8 | 60 | 0.30 | 8.51 | 27.01 |
| 100 | 8 | 72 | 0.36 | 10.21 | 30.42 |
| 100 | 8 | 84 | 0.42 | 11.91 | 33.82 |
| 100 | 8 | 96 | 0.48 | 13.61 | 37.22 |
| 100 | 8 | 108 | 0.54 | 15.31 | 40.63 |
| 100 | 8 | 120 | 0.60 | 17.01 | 44.03 |

Appendix 2

Table 7 Accuracy of model NBC-I

| Rebar condition | Rust grade | Rust rate α | β range | Correct number | Accuracy |
|-----------------|------------|--------------------------|-----------------------|----------------|----------|
| No rust | 1 | $0 \leq \alpha < 0.02$ | $0 \leq \beta < 0.02$ | 0 | 100.0% |
| Slight rust | 2 | $0.02 \leq \alpha < 0.1$ | $0.02 \leq \beta < 1$ | 10 | 83.3% |
| Moderate rust | 3 | $0.1 \leq \alpha < 0.2$ | $1 \leq \beta < 3$ | 14 | 77.8% |
| Severe rust | 4 | $0.2 \leq \alpha \leq 1$ | $\beta \geq 3$ | 20 | 83.3% |
| Total | | | | 44 | 81.5% |

Table 8 Accuracy of model NBC-II

| Rebar condition | Rust grade | Rust rate α | γ range | Correct number | Accuracy |
|-----------------|------------|--------------------------|-------------------------|----------------|----------|
| No rust | 1 | $0 \leq \alpha < 0.02$ | $0 \leq \gamma < 0.2$ | 0 | 100.0% |
| Slight rust | 2 | $0.02 \leq \alpha < 0.1$ | $0.2 \leq \gamma < 0.4$ | 11 | 91.6% |
| Moderate rust | 3 | $0.1 \leq \alpha < 0.2$ | $0.4 \leq \gamma < 0.9$ | 10 | 56.6% |
| Severe rust | 4 | $0.2 \leq \alpha \leq 1$ | $\gamma \geq 0.9$ | 22 | 91.7% |
| Total | | | | 43 | 79.6% |

Table 9 Accuracy of model NBC-III

| Rebar condition | Rust grade | Rust rate α | β and γ range | Correct number | Accuracy |
|-----------------|------------|--------------------------|--|----------------|----------|
| No rust | 1 | $0 \leq \alpha < 0.02$ | $0 \leq \beta < 0.02$ or $0 \leq \gamma < 0.2$ | 0 | 100.0% |
| Slight rust | 2 | $0.02 \leq \alpha < 0.1$ | $0.02 \leq \beta < 1$ or $0.2 \leq \gamma < 0.4$ | 11 | 91.7% |
| Moderate rust | 3 | $0.1 \leq \alpha < 0.2$ | $1 \leq \beta < 3$ or $0.4 \leq \gamma < 0.9$ | 15 | 83.3% |
| Severe rust | 4 | $0.2 \leq \alpha \leq 1$ | $\beta \geq 3$ or $\gamma \geq 0.9$ | 23 | 95.6% |
| Total | | | | 49 | 90.7% |

Tables 7, 8, 9

Abbreviations

| | |
|---------|--|
| SMFL | Spontaneous magnetic flux leakage |
| NBC | Naive Bayesian models |
| NDT | Nondestructive Testing |
| L-C-R-W | Length-concrete thickness-diameter-rust width |
| PLC | Programmable logic controllers |
| LFH | Lift-off height |
| B_x | Magnetic induction intensity along x direction |
| B_y | Magnetic induction intensity along y direction |
| B_z | Magnetic induction intensity along z direction |

Acknowledgements

All authors thank the anonymous reviewers for constructive comments that helped improve this manuscript.

Authors' contributions

"YH" and "LS" supervised the work in this manuscript and gave guidelines to achieve the goal of this manuscript. The authors read and approved the final manuscript.

Funding

This research did not receive any specific grant from funding agencies in the public, commercial, or not-for-profit sectors.

Availability of data and materials

All data generated or analyzed during this study are included in this published article.

Declarations**Competing interests**

The authors declare that they have no competing interests.

Received: 22 September 2022 Accepted: 14 December 2022

Published online: 07 January 2023

References

1. Fernandes B, Titus M, Karl Nims D et al (2012) Field test of magnetic methods for corrosion detection in prestressing strands in adjacent box-beam bridges. *J Bridg Eng* 17(6):984–988
2. Shi PP, Su SQ, Chen ZM (2020) Overview of researches on the nondestructive testing method of metal magnetic memory: status and challenges. *J Nondestruct Eval* 39(8):83–92
3. Bao S, Jin P, Zhao Z et al (2020) A review of the metal magnetic memory method. *J Nondestruct Eval* 39(3):196–199
4. Shi CL, Dong SY, Xu BS et al (2010) Metal magnetic memory effect caused by static tension load in a case-hardened steel. *J Magn Magn Mater* 322(4):413–416
5. Guo W, Dong LH, Bin-Shi XU et al (2016) Research status and progress of active infrared thermographic nondestructive testing. *Nondestructive Testing*
6. Wronkiewicz-Katunin A, Dragan K (2020) Impact damage evaluation in composite structures based on fusion of results of ultrasonic testing and X-ray computed tomography. *Sensors* 20(7):1867
7. Leng JC, Yang L, Zhou G et al (2013) Metal magnetic memory signal response to plastic deformation of low carbon steel. *NDT E Int* 55:42–46
8. Withers PJ, Turski M, Edwards L et al (2008) Recent advances in residual stress measurement. *Int J Press Vessel Pip* 85(3):118–127
9. Orbe A, Rojí E, Losada R et al (2014) Calibration patterns for predicting residual strengths of steel fibre reinforced concrete (SFRC). *Composites Part B* 58(58):408–417
10. Zhang H, Liao L, Zhao RQ, Zhou J, Yang M, Xia R (2016) The nondestructive test of steel corrosion in reinforced concrete bridges using a micro-magnetic sensor. *Sensors* 16:1439
11. Zhang J, Liu C, Sun M et al (2017) An innovative corrosion evaluation technique for reinforced concrete structures using magnetic sensors. *Constr Build Mater* 135(MAR.15):68–75
12. Polydorides N, Georgiou GE, Kim DH et al (2008) Subspace constrained regularization for corrosion detection with magnetic induction tomography. *NDT E Int* 41(7):510–516
13. Sun B, Ping D, Chong W et al (2009) Quantitative analysis of magnetic anomaly of reinforcements in bored in-situ concrete piles. *Appl Geophys* 6(3):275–286
14. Szielasko K, Youssef S, Sourkov A et al (2015) Magnetic flux leakage detection of corrosion damage in prestressed concrete poles. *Electromagnetic Nondestruct Eval (XVIII)* 40(5):203–210
15. Titus M (2013) Practical assessment of magnetic methods for corrosion detection in an adjacent precast, prestressed concrete box-beam bridge. *Nondestruct Testing Eval* 28(2):99–118
16. Gaydecki P, Fernandes B, Quek S et al (2007) Inductive and magnetic field inspection systems for rebar visualization and corrosion estimation in reinforced and pre-stressed concrete. *Nondestruct Testing Eval* 22(4):255–298
17. Benitez DS, Quek S, Gaydecki P et al (2008) A preliminary magnetoinductive sensor system for real-time imaging of steel reinforcing bars embedded within concrete. *IEEE Trans Instrum Meas* 57(11):2437–2442
18. Zhang YL, Gou RB, Li JM et al (2012) Characteristics of metal magnetic memory signals of different steels in high cycle fatigue tests. *Fatigue Fract Eng Mater Struct* 35(7):595–605
19. Liu B, Xue X, Li J et al (2019) Grain size effect on metal magnetic memory signal for stress damage evaluation of low carbon steel. *Nondestruct Testing Eval* 34(3):267–282
20. Pang C, Zhou J, Zhao Q et al (2019) A new method for internal force detection of steel bars covered by concrete based on the metal magnetic memory effect. *Metals* 9(6):661
21. Pang C, Zhou J et al (2019) Research on internal force detection method of steel bar in elastic and yielding stage based on metal magnetic memory. *Materials* 12(7):1167
22. Yang D, Qiu J, Di H et al (2019) Quantitative evaluation of corrosion degrees of steel bars based on self-magnetic flux leakage. *Metals* 9(9):952
23. Zhao Q, Zhou J, Xia Q et al (2019) Non-destructive testing of steel corrosion fluctuation parameters based on spontaneous magnetic flux leakage and its relationship with steel bar diameter. *Materials* 12(24):4116
24. Breiman L, Friedman J, Olshen R A, et al. Classification and regression trees[M]. Belmont: Wadsworth, 2004, 32(8).
25. Niuniu X, Yuxun L. (2010) Notice of retraction: review of decision trees[C]//2010 3rd international conference on computer science and information technology. IEEE 5:105–109

26. Bo Y, Yang LF, Li B (2014) Practical model for predicting corrosion rate of steel reinforcement in concrete structures. *Constr Build Mater* 54(54):385–401
27. Xia R, Zhang H, Zhou J et al (2020) Probability evaluation method of cable corrosion degree based on self-magnetic flux leakage. *J Magn Magn Mater* 522:167544

Publisher's Note

Springer Nature remains neutral with regard to jurisdictional claims in published maps and institutional affiliations.

Submit your manuscript to a SpringerOpen[®] journal and benefit from:

- Convenient online submission
- Rigorous peer review
- Open access: articles freely available online
- High visibility within the field
- Retaining the copyright to your article

Submit your next manuscript at ► [springeropen.com](https://www.springeropen.com)
